J. Fluid Mech. (1982), *vol.* 118, *pp.* 79–107
Printed in Great Britain

Vortex–leading-edge interaction

By SAMIR ZIADA† AND DONALD ROCKWELL
Department of Mechanical Engineering and Mechanics, Lehigh University,
Bethlehem, Pa. 18015, U.S.A.

(Received 23 February 1981 and in revised form 30 September 1981)

Visualization of successive vortices impinging upon the leading edge of a wedge reveals patterns of deformation of each incident vortex; for certain offsets of the edge with respect to the incident vortex there is pronounced vortex shedding from the leading edge, whereby the shed vortex has a vorticity orientation opposite to that of the incident vortex.

Simultaneous consideration of this visualization interaction and the force induced on the wedge gives the relation between the nature of the interaction mechanism and the relative magnitude and phase of the force exerted on the wedge. The amplitude of the induced force is found to be a strong function of the transverse offset of the leading edge with respect to the incident vortex and the degree of vorticity shedding from the leading edge. Application of Stuart's vortex model to the incident vortices provides a means for approximating the phase and relative amplitude of the induced force as a function of the transverse offset of the leading edge.

1. Introduction

A key feature of many noise-generation and structural-loading problems is the interaction of an incident vortical structure(s) with the leading edge of a plate, wedge or airfoil. In the case of sound production, it is well-known that the character of the far-field sound can be related to the nature of the local hydrodynamics; that is, in the event that an incident vortical structure, or eddy, is 'compact', and the solid surface associated with the leading edge is compact as well, the far-field sound is linked directly to the local hydrodynamics in the vicinity of the leading edge (Crighton 1975). Such impingement of vortices has special significance for the broad class of flows involving oscillations of impinging shear layers (Rockwell & Naudascher 1979), including jet–edge and mixing-layer–edge configurations. In these cases, the upstream influence arising from the unsteady-flow–leading-edge interaction is central to ensuring that such oscillations are self-sustaining. That is, pressure and velocity fluctuations in the vicinity of the edge are manifested in vorticity fluctuations in the sensitive region of the shear layer near the upstream separation boundary; these vorticity fluctuations are, in turn, amplified, closing the loop for the self-sustaining oscillation process. Concerning the local loading of edge-type or airfoil-type geometries, local forces, if compact, can be related to dipole-type sources; aside from this acoustical aspect and possible upstream influence, the dynamics associated with the impingement of a vortical structure or a complex combination of vortices, giving rise to finite perturbations at the leading edge of an airfoil, is a problem of fundamental importance. Clearly,

---

† Present address: Lab. for vibrations and acoustics, Sulzer Bros, Winterthur, Switzerland.

the detailed mechanics of the leading-edge interaction must be understood fully if the unsteady loading is to be described. In this regard, the nature of this interaction is expected to be a strong function of the structure and positioning of the incident vortex.

Vortex–solid-boundary interaction has been modelled for a variety of configurations using line vortices. Crighton (1975) reviews work on two such configurations: impingement of a pair of vortices having opposite circulations upon a flat plate, and motion of a line vortex around the edge of a rigid half-plane. In addition, Rogler (1974) examines the interaction of a line vortex with the leading edge of a flat plate. Finally, Conlisk & Rockwell (1981) describe the case of line-vortex impingement upon a corner. In all of these investigations, the trajectory of the vortex or vortices is of primary importance and the implicit assumption is that the distributed vorticity of the laboratory vortices can be modelled effectively by using line vortices having appropriate strength; moreover, it is also implicit that the distributed vorticity remains intact, not experiencing varying degrees of distention or severing at an edge as described by Rockwell & Knisely (1979).

The impingement of distributed vorticity upon the leading edge of a flat plate has been analysed by Rogler (1978) for the special case of an array of inviscid 'square-type' vortices, giving a continuous distribution of vorticity throughout the flow. According to Rogler, in the region very near the leading edge, the nonlinear rearrangement of vorticity will be significant; however, he contends that this region is small provided the free-stream disturbances are sufficiently weak, justifying the linear assumptions of his analysis. Moreover, the role of local viscous effects, especially with regard to their unsteady influence at a sharp leading edge, has remained unclear. The existence of a pressure singularity at the leading edge in Rogler's analysis suggests that local separation, in the form of leading-edge vortex shedding at a rate compatible with the incident disturbances may occur; if this shedding from the leading edge of a semi-infinite plate involves vorticity of an opposite sign to that of the incident vorticity, then leading-edge viscous effects must indeed play a role. In essence, it is evident that the extent to which nonlinear and viscous effects influence the leading-edge dynamics remains unresolved for realistic concentrations of incident vorticity; experimental insight is essential.

The present investigation examines experimentally the interaction of a row of vortices with the leading edge of a wedge, whereby the vortex has a defined structure at a reference location upstream of the leading edge. Attention is focussed on the interaction mechanism near the leading edge, which is strongly influenced by the position of the leading edge relative to the incident vortex, and, in most cases, is quite different from what would be expected on the basis of inviscid analyses similar to the aforementioned.

2. Experimental system

Figure 1 shows an overall view of the experimental test section, including the approach flow configuration for generating the mixing layer, the impingement wedge and force measurement system, as well as the lighting system for visualization. Concerning the approach flow, it was divided into two streams upstream of the test section, with the low-speed side experiencing a pressure drop through a honeycomb arrangement (not shown in figure 1). By proper design of the contour of the splitter plate between the two

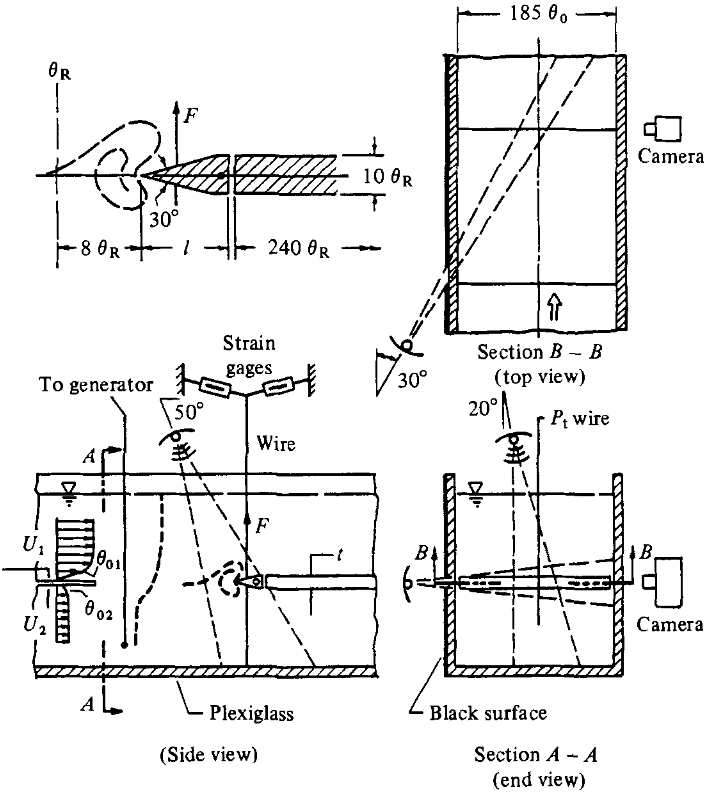

FIGURE 1. Overall view of the experimental test section, lighting arrangement for flow visualization using hydrogen bubbles, and close-up view of wedge.

streams, both the high- and low-speed streams experienced a mildly favourable streamwise pressure gradient, thereby avoiding instability of the boundary layer that would lead to transition. Consequently, the conditions at the trailing edge of the splitter plate involved a free-stream velocity of 18·35 cm/s at the high-speed side (U_1), velocity ratio $U_1/U_2 = 2{\cdot}85 \pm 0{\cdot}05$, and laminar boundary layers having momentum thicknesses $\theta_{01} = 0{\cdot}62$ mm and $\theta_{02} \simeq 0{\cdot}68$ mm, θ_0 being their sum. The corresponding Reynolds number was $R_{\theta_0} = (U_1 - U_2)\theta_0/\nu = 157$ or $R_{\theta R} = (U_1 - U_2)\theta_R/\nu = 230$, where θ_R is the local momentum thickness at the streamwise station $11\theta_0$ upstream of the leading edge of the wedge. Separation of these layers led to the formation of extremely well-defined vortices that eventually impinged upon a 30° wedge of length l, a close-up view of which is shown in figure 1. To preclude parasitic effects associated with vortex shedding from the downstream part of the wedge, a very long ($l' = 240\theta_R$) plate was provided as indicated. Other relevant dimensions of the system were: $b/\theta_0 \equiv$ thickness of trailing edge $= 3$; $t/\theta_0 \equiv$ thickness of impingement wedge $= 15$; and $L/\theta_0 \equiv$ length from trailing edge to impingement wedge $= 15$–150.

Force fluctuations were measured using a high-sensitivity transducer system involving two sets of four strain gauges attached to both branches of the Y-shaped wire, which was kept under tension. As shown in figure 1, the vertical portion of the wire arrangement held the wedge (i.e. the sensitive leading part of the impingement plate) in the mid-position. All strain gauges were connected in series and formed one

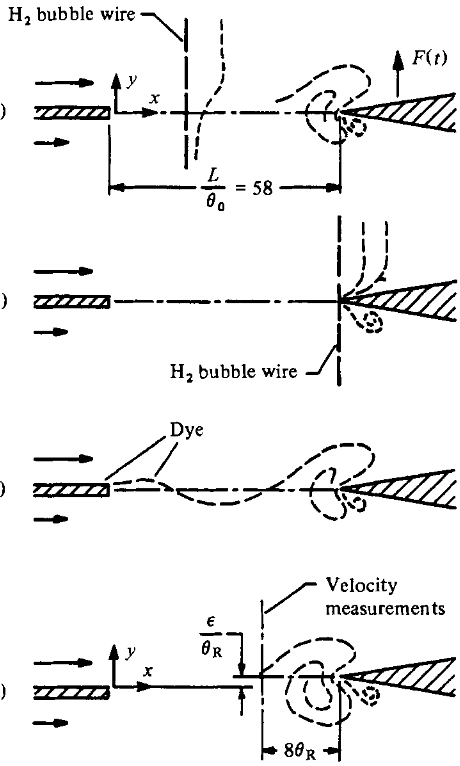

FIGURE 2. Schematic illustrating various methods of visualization and terminology for vortex–leading-edge interaction.

arm of a Wheatstone-bridge arrangement. The resultant voltage fluctuations due to force fluctuations were amplified and filtered (at zero-phase shift setting) before being displayed on a storage oscilloscope. Tests to determine the natural frequency of the wedge system revealed it to be 14·5 Hz, which is a factor 4·5 above the highest frequency of interest in this investigation. Amplitude and phase distortion were estimated to be 5 % and 1·9 degrees respectively.

Visualization was carried out using hydrogen-bubble and dye-injection methods, as described subsequently. The lighting arrangement, particularly critical for effective bubble contrast, is depicted in figure 1. A 90 W stroboscopic light (Instrobe 90) having a flash duration of 10 μs, and operating at a trigger frequency of 120 Hz, illuminated the bubble sheet from above at the angles indicated. Simultaneously, a 1000 W constant (quartz) light source was directed through a slit in the side of the test section as indicated. In the case of visualization by the dye injection method, the constant 1000 W source was placed on the opposite side of the test section from the television camera, and the stroboscopic light was not employed. Moreover, the black surface was removed, and a sheet of translucent paper placed on the vertical side of the test section to diffuse the incident light.

The time-dependent evolution of the visualized vortex–wedge interaction and the instantaneous-force fluctuation (displayed on a storage oscilloscope) were recorded simultaneously on a split-screen Instar television system having vertical and horizontal sweep frequencies of 120 Hz and 25·2 kHz, a resolution of 250 lines, and a framing rate of 120 frames/s. The uncertainty due to the finite time between frames on the videotape was ± 3 % of the period of vortex formation. Photos shown herein were obtained by taking 4 in. × 5 in. Polaroids of the image on the video screen. At this point, it is appropriate to comment on the relative scale of the flow-visualization photos to be discussed subsequently; the '*a*' series of photographs corresponding to figures 4–8, i.e. 4(*a*), 5(*a*), have the same scale; likewise the '*b*' series of photos have a common scale, though the scale differs from that in series '*a*'. Series '*c*' does not have a common scale. The fact that series '*a*' and '*b*' each have a common scale facilitates direct quantitative comparison between the photos at different values of offset.

As shown in the schematic of the overall flow-visualization facility of figure 1, hydrogen bubbles were generated from a vertical 0·05 mm platinum wire, which could be positioned well upstream of the impingement edge (figure 2*a*), and very close to the edge (figure 2*b*), allowing examination of the upstream nature of the flow as well as revealing local dynamics in the immediate vicinity of the edge. Using a tuneable pulse generator, timelines of hydrogen bubbles could be generated. For the case where the hydrogen bubble wire was located a distance of $21\theta_{\rm R}$ upstream of the impingement edge, the streamwise growth of each vortex, and its eventual impingement on the edge, could be clearly observed. On the other hand, by placing the wire at the impingement edge, the vortex shed from the underside of the leading edge could be particularly well characterized. Furthermore, this wire location brought out the changes in concentration of vorticity of the incident vortical structure that occurred downstream of the leading edge. In addition to this method, the dye-injection technique, involving placement of a layer of food colouring on the upper surface of the trailing edge, allowed generation of continuous streakline patterns (figure 2*c*); this technique was particularly valuable in providing complementary insight into vortex shedding from the leading edge. Taken together, these three methods of visualizing the interaction mechanism provide composite insight into the leading-edge region. In figure 2(*d*), terminology employed in subsequent discussion is defined. Particularly important is the dimensionless transverse offset of the leading edge $\epsilon/\theta_{\rm R}$, in which $\theta_{\rm R}$ represents the reference momentum thickness measured just upstream of the leading edge.

3. Nature of incident vortex

For the free shear layer upstream of the wedge, Stuart's (1967) exact solution of the inviscid vorticity equation can be used to approximate the structure of the incident vortex. This model accommodates variable concentrations of continuously distributed vorticity in the form of a constant α. In a frame of reference moving at speed $-U_{\rm a}$ in the x-direction, the expressions for the streamwise (u) and transverse (v) velocities are

$$u = U_{\rm a} + \frac{\sinh(2\pi y/\lambda)}{\cosh(2\pi y/\lambda) + \alpha\cos(2\pi[x - U_{\rm a}t]/\lambda)}, \tag{1}$$

$$v = \frac{\alpha\sin(2\pi[x - U_{\rm a}t]/\lambda)}{\cosh(2\pi y/\lambda) + \alpha\cos(2\pi[x - U_{\rm a}t]/\lambda)}. \tag{2}$$

As shown schematically in figure 3(*a*), u approaches $U_{\rm a} \pm 1$ as y approaches $\pm\infty$. At $t = \lambda/2U_{\rm a}$, vortex centres are located at $y = 0, x = 0, \pm\lambda, \pm 2\lambda, \ldots$. To determine the magnitudes of the velocity fluctuation components at the frequency of passage of the vortices, $\tilde{u}_{\rm rms}(\beta)$ and $\tilde{v}_{\rm rms}(\beta)$, as well as at the first harmonic, $\tilde{u}_{\rm rms}(2\beta)$ and $\tilde{v}_{\rm rms}(2\beta)$,

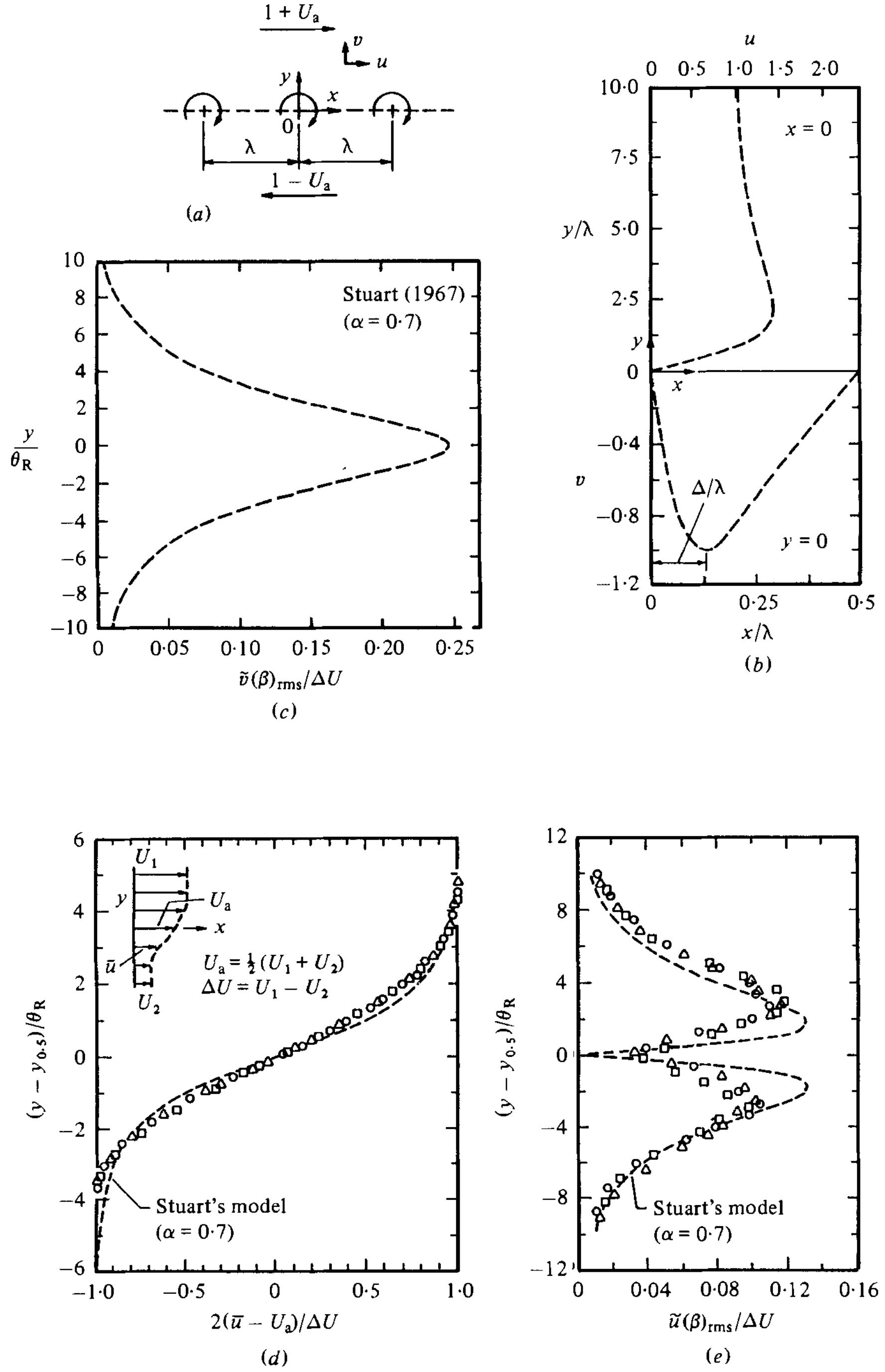

FIGURE 3. Features of Stuart's (1967) vortex model ($\alpha = 0\cdot7$): (*a*) vortex row; (*b*) distributions of transverse and streamwise velocities for $U_a = 0$ showing $u(y/\lambda)$ along $x = 0$ and $v(x/\lambda)$ along $y = 0$; (*c*) distribution of time-averaged transverse fluctuation velocity amplitude $\tilde{v}(\beta)_{rms}$. Characteristics of incident vortex measured at reference station $8\theta_R$ upstream of the leading edge of the wedge and comparison with Stuart vortex model: (*d*) mean-velocity profile $\bar{u}(y)$; (*e*) distribution of streamwise fluctuation velocity $\tilde{u}(\beta)_{rms}$. ○, $\epsilon/\theta_R = 1\cdot2$; △, -1; □, $-2\cdot6$.

spectral analysis of the instantaneous velocity components $u(t)$ and $v(t)$ was carried out for both Stuart's model and the hot-film anemometry signal. This involved digitizing the time-dependent velocity signal and taking its Fourier transform (FFT). To improve accuracy, a 4-term Blackman–Harris window was used.

Figure 3(*b*) shows typical distributions of instantaneous velocities $u(y/\lambda)$ at $x = 0$ and $v(x/\lambda)$ at $y = 0$ for the vortex model having vorticity concentration corresponding to $\alpha = 0{\cdot}7$; this choice is to be justified subsequently. Note that the maximum negative value of v occurs at a distance $\Delta/\lambda \simeq 0{\cdot}125$ from the centre of the vortex. This length scale Δ/λ will be shown to have special significance with regard to the phasing of the maximum negative force on the wedge.

The time-mean velocity $\bar{u}$ can be found by integrating (1) over a wavelength λ. This leads to

$$\bar{u} = U_a + \frac{\sinh(2\pi y/\lambda)}{[1-\alpha^2+\sinh^2(2\pi y/\lambda)]^{\frac{1}{2}}}. \tag{3}$$

In addition, the reference momentum thickness is defined as

$$\theta_R = \int_{-\infty}^{\infty} \left[\frac{1}{4} - \left(\frac{\bar{u}-U_a}{\Delta U}\right)^2\right] dy, \tag{4}$$

where U_1 and U_2 are the free-stream components on the high- and low-speed sides of the mean shear layer, $\Delta U = U_1 - U_2$ represents their difference, and $U_a = \frac{1}{2}(U_1+U_2)$ their average; the co-ordinate $y_{0{\cdot}5}$ is defined as the value of y at $\bar{u} = U_a$.

Figure 3(*c*) shows the distribution of the transverse velocity component $\tilde{v}_{\text{rms}}(\beta)$. At each value of y/θ_R, the value of $\tilde{v}_{\text{rms}}(\beta)$ was determined from the aforementioned spectral analysis. It is evident that small variations in y, of the order of local momentum thickness θ_R, can be associated with substantial changes in the amplitude of $\tilde{v}_{\text{rms}}(\beta)$. Comparison of the calculated and measured distributions of mean velocity is given in figure 3(*d*). Measurements were taken at a distance of $8\theta_R$ upstream of the leading edge of the wedge. With regard to the mean-velocity profile predicted by the model, Stuart (1967) has shown that extreme choices of vorticity concentration parameter of $\alpha = 0{\cdot}1$, $1{\cdot}0$ produce nearly congruent distributions; if superposed on the distribution of figure 3(*d*) (calculated for $\alpha = 0{\cdot}7$) the three distributions would be nearly indistinguishable. The data shown in figure 3(*d*) were taken for three different values of wedge offset ϵ/θ_R, corresponding to extreme and intermediate values considered subsequently in the flow-visualization study. With each distribution referenced to its local $y_{0{\cdot}5}$ value, the distributions are remarkably coincident.

Figure 3(*e*) compares the distribution of $\tilde{u}_{\text{rms}}(\beta)$, for the same values of wedge offset. Again, the distributions are coincident, and are well-approximated by the predicted distributions corresponding to $\alpha = 0{\cdot}7$. As discussed by the authors (Ziada & Rockwell 1981), this invariance of the unsteady velocity distribution is associated with the saturation of the fluctuation velocity amplitudes for all values of ϵ at locations upstream of the measurement station. So, in summary, the fact that mean- and fluctuating-velocity distributions (shown in figures 3*d*,*e*) associated with the incident vortex are not significantly altered provides a consistent set of initial conditions for various values of offset of the wedge with respect to the incident vortex.

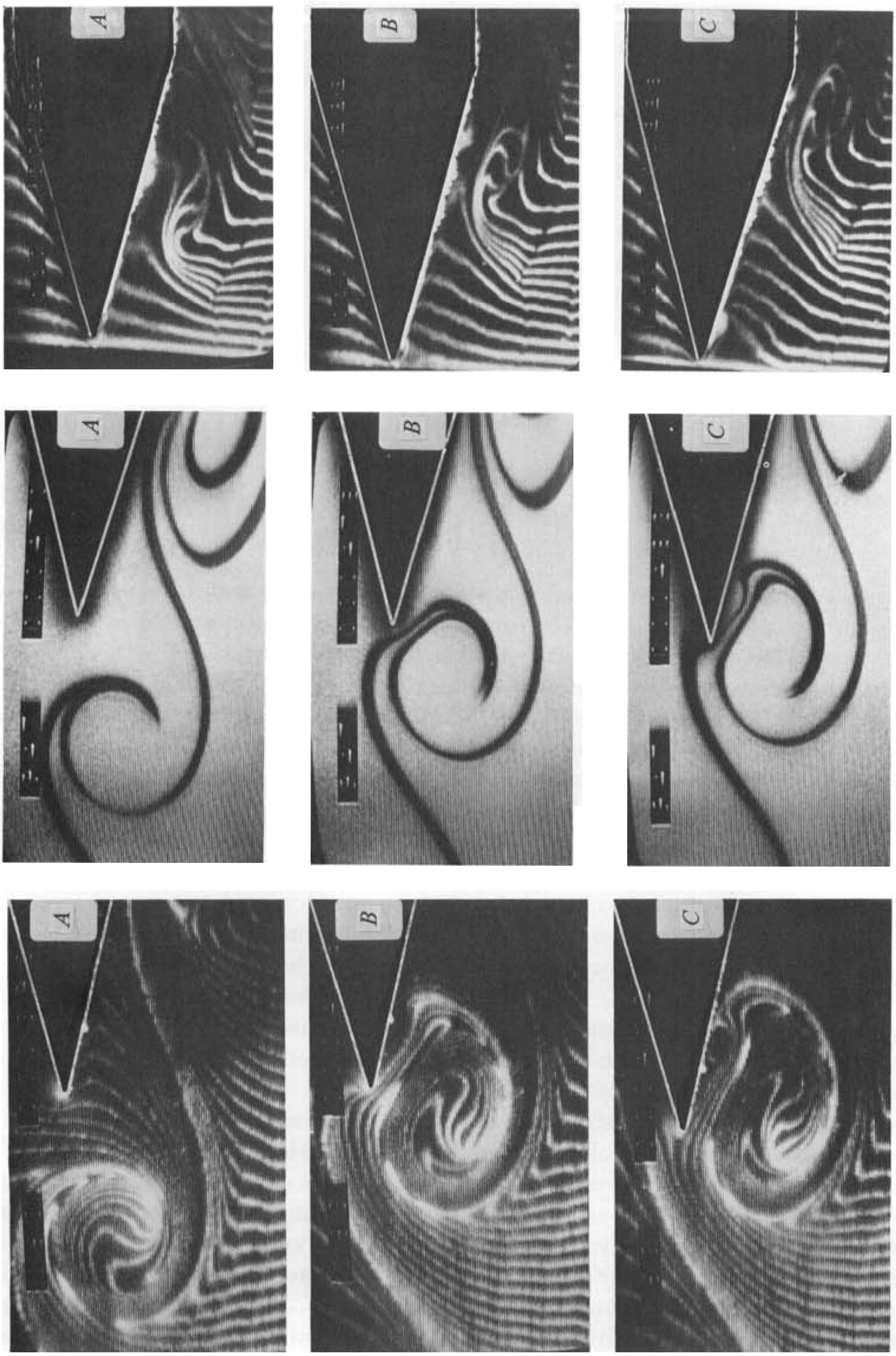
A
B
C
A
B
C
A
B
C

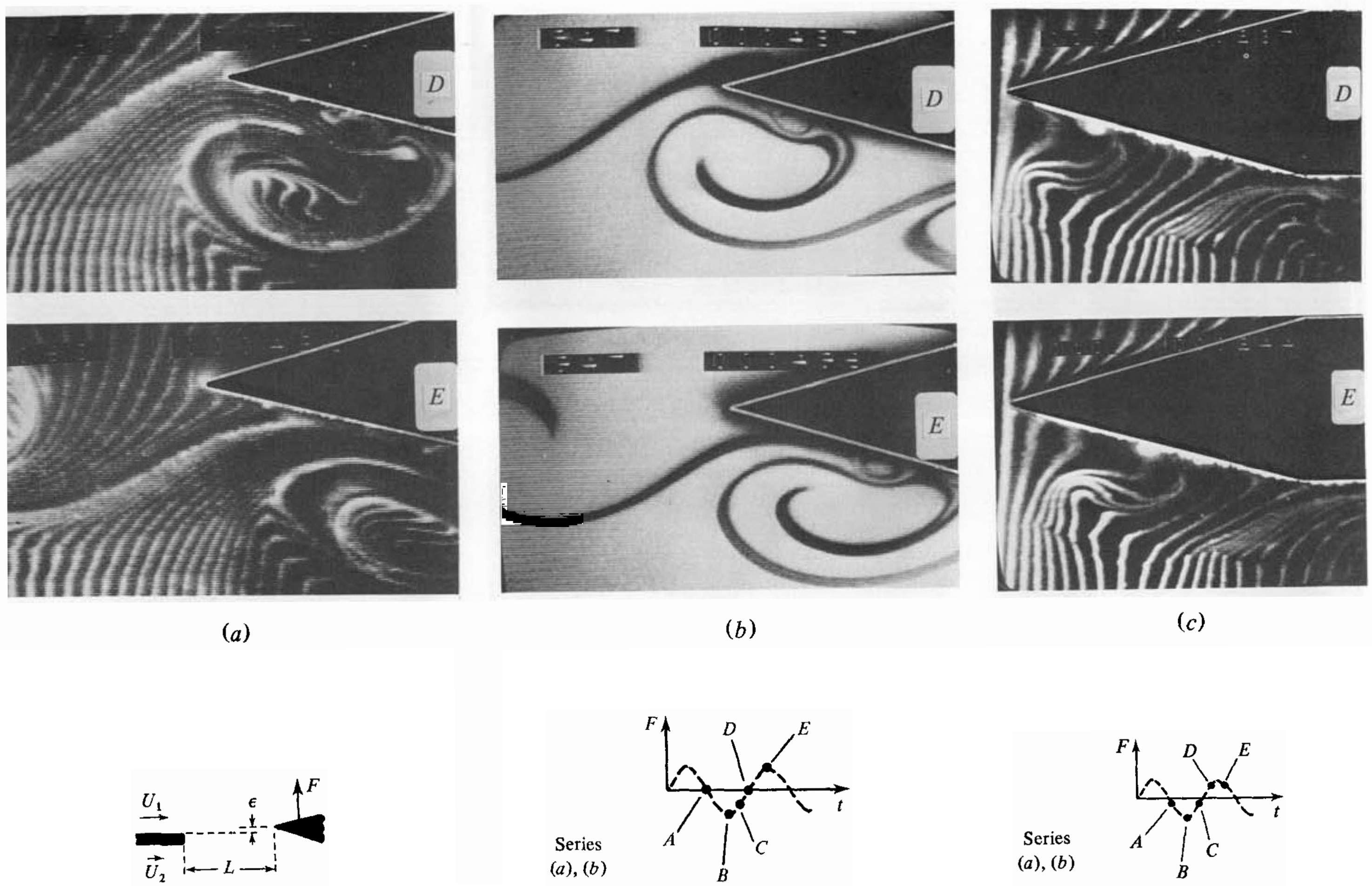

FIGURE 4. Visualization of vortex–leading-edge interaction for: (*a*) hydrogen-bubble wire located $21\theta_R$ upstream of wedge; (*b*) dye marker emanating from top edge of splitter plate; (*c*) wire located at leading edge. $R_{\theta_R} = \Delta U\theta_R/\nu = 230$, $\epsilon/\theta_R = 1{\cdot}2$, $L/\theta_R = 58$.

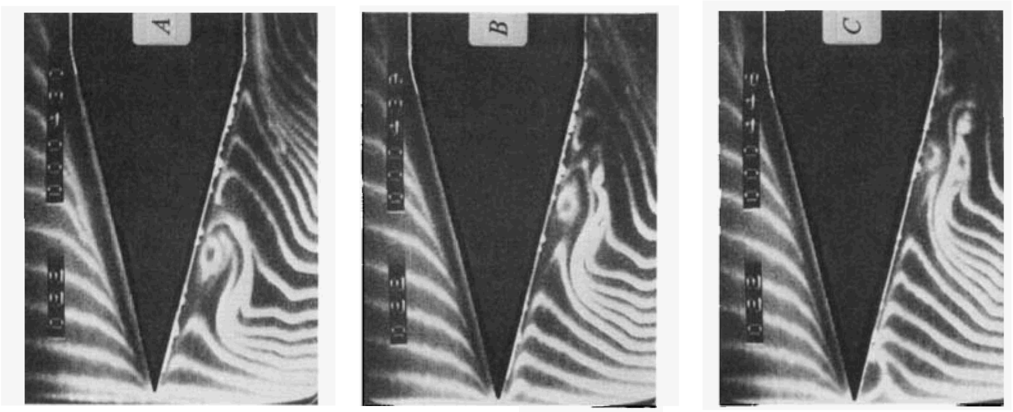
A
B
C

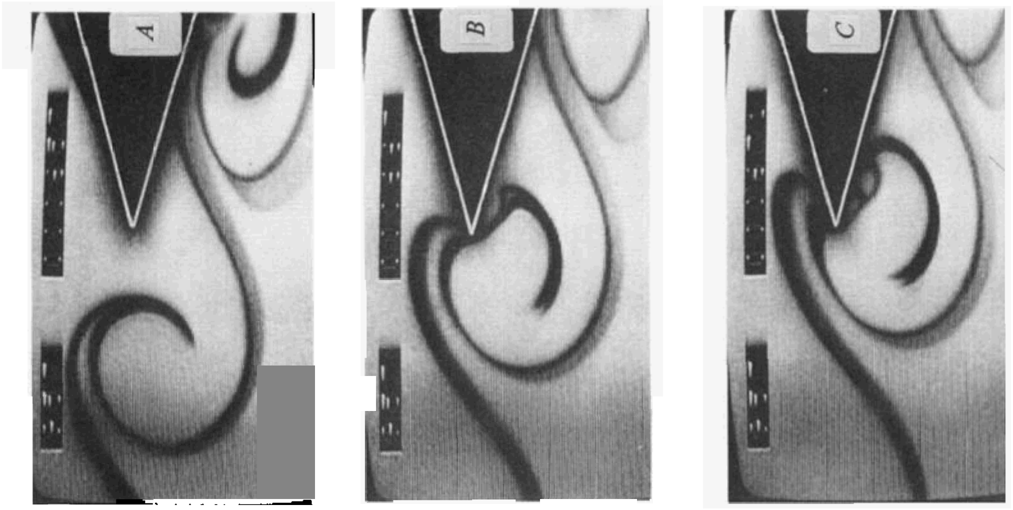
A
B
C

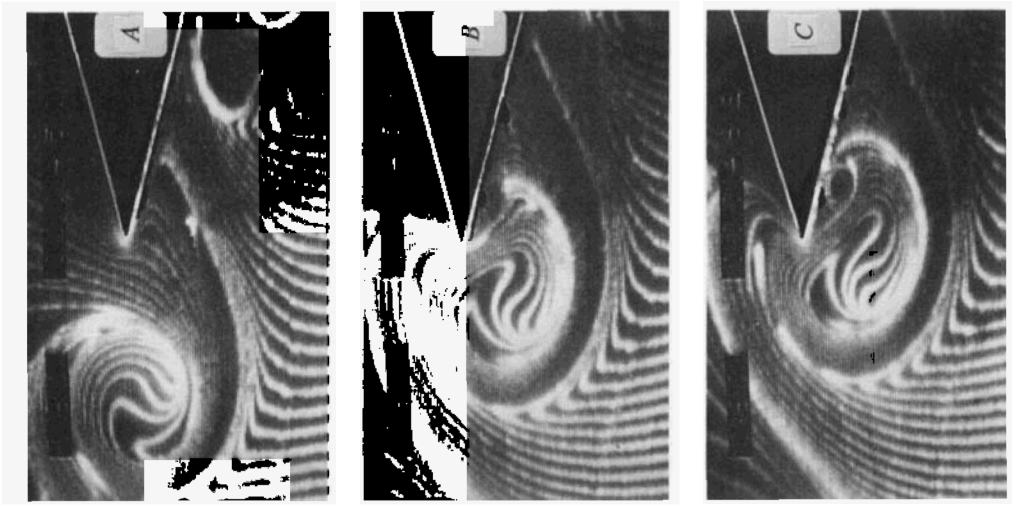
A
B
C

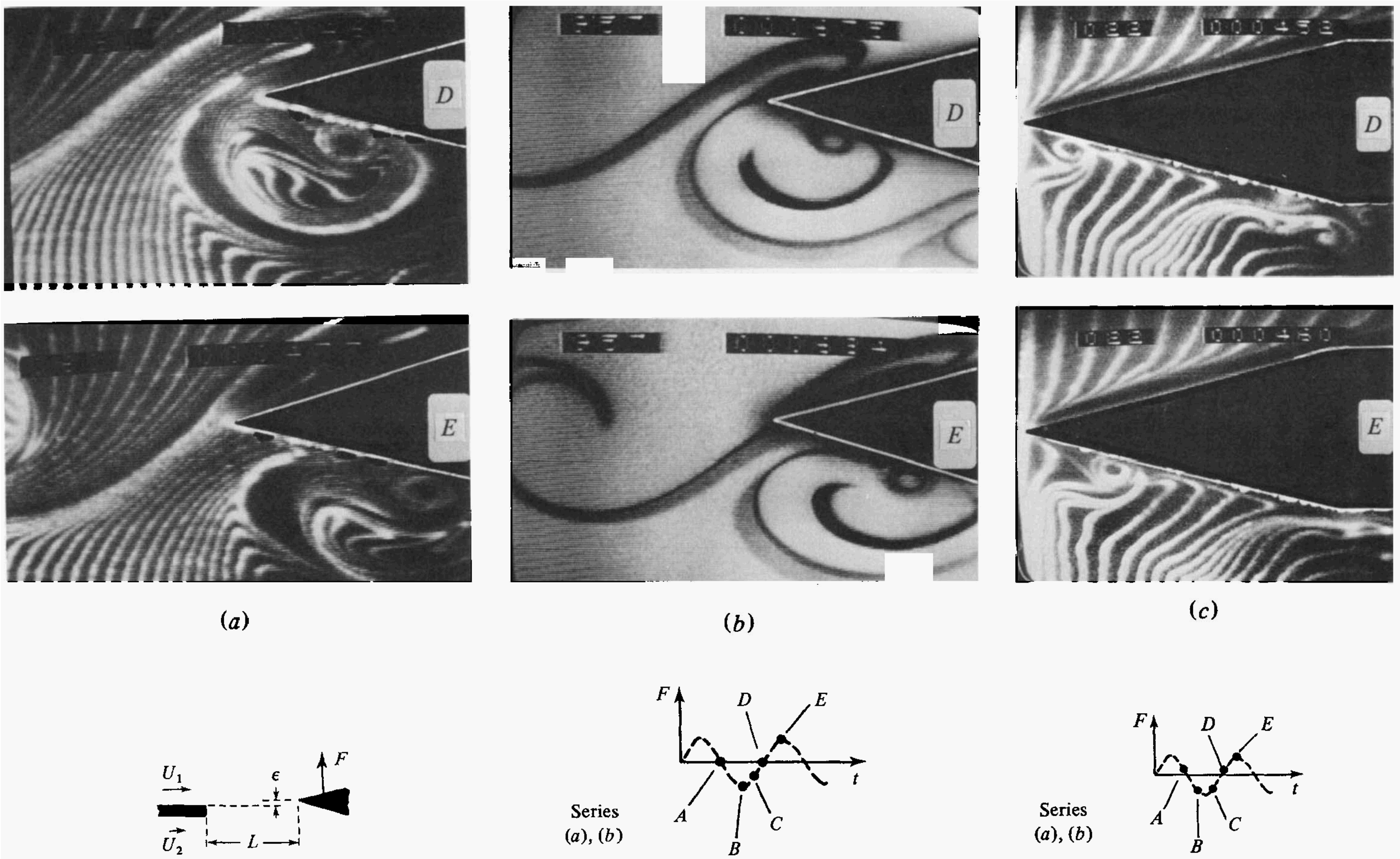

Figure 5. Visualization of vortex–leading-edge interaction for: (*a*) hydrogen-bubble wire located $21\theta_{\mathrm{B}}$ upstream of wedge; (*b*) dye marker emanating from top edge of splitter plate; (*c*) wire located at leading edge. $R_{\theta_{\mathrm{B}}} = 230$, $\epsilon/\theta_{\mathrm{B}} = 0{\cdot}2$, $L/\theta_{\mathrm{B}} = 58$.

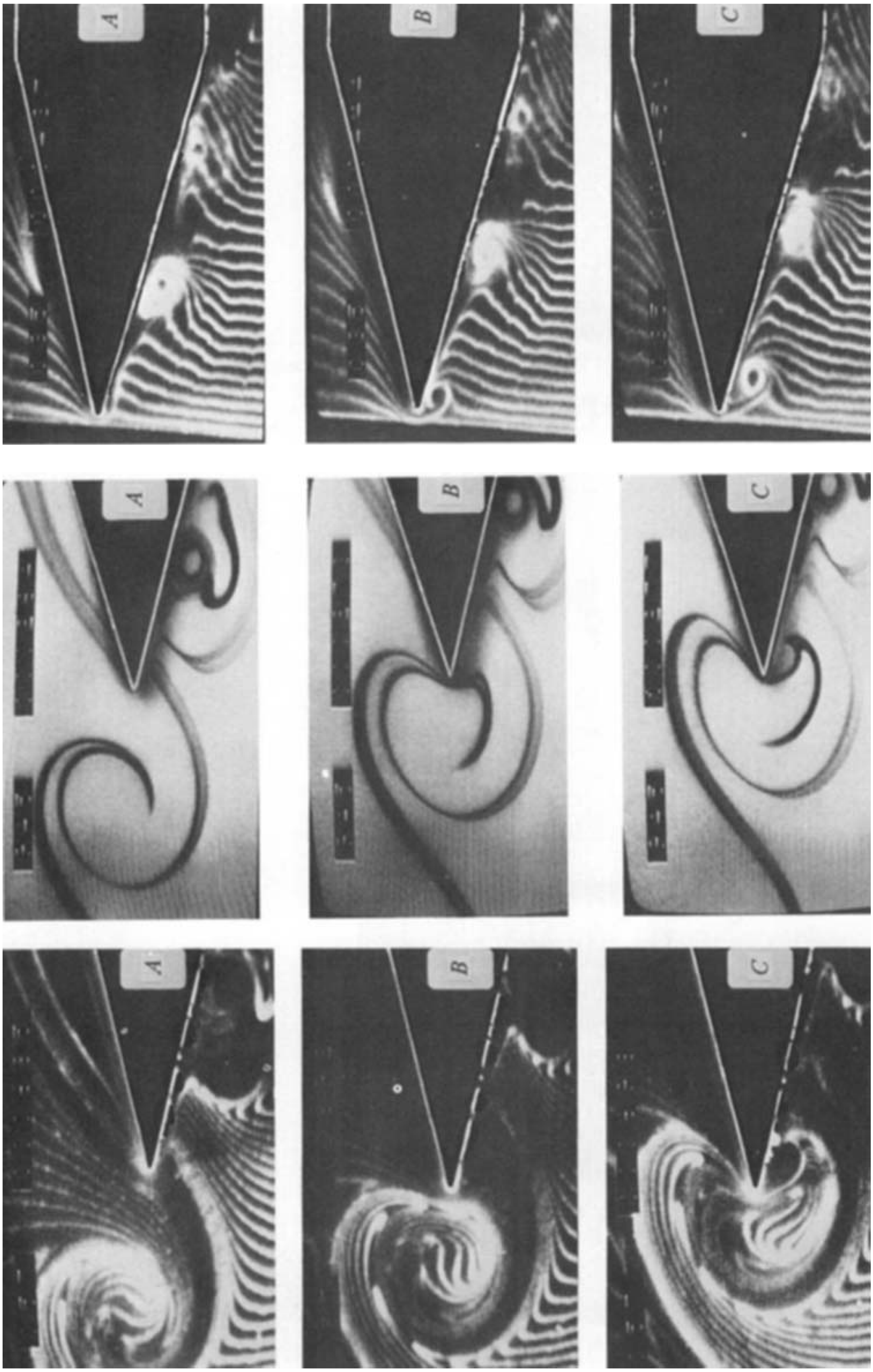
A
B
C
A
B
C
A
B
C

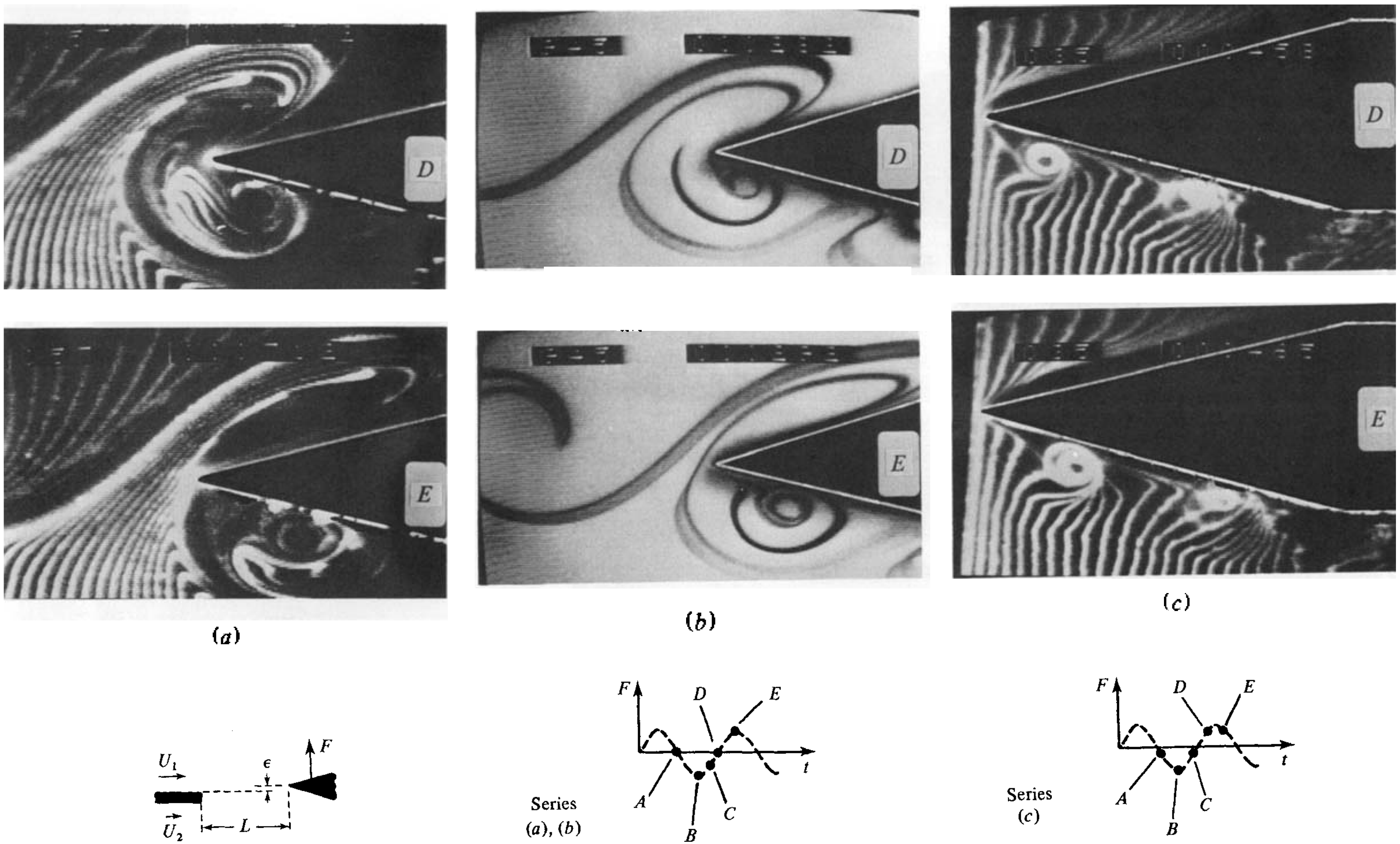

FIGURE 6. Visualization of vortex–leading-edge interaction for: (a) hydrogen-bubble wire located $21\theta_R$ upstream of wedge; (b) dye marker emanating from top edge of splitter plate; (c) wire located at leading edge. $R_{\theta_R} = 230$; $\epsilon/\theta_R = -1{\cdot}0$, $L/\theta_0 = 58$.

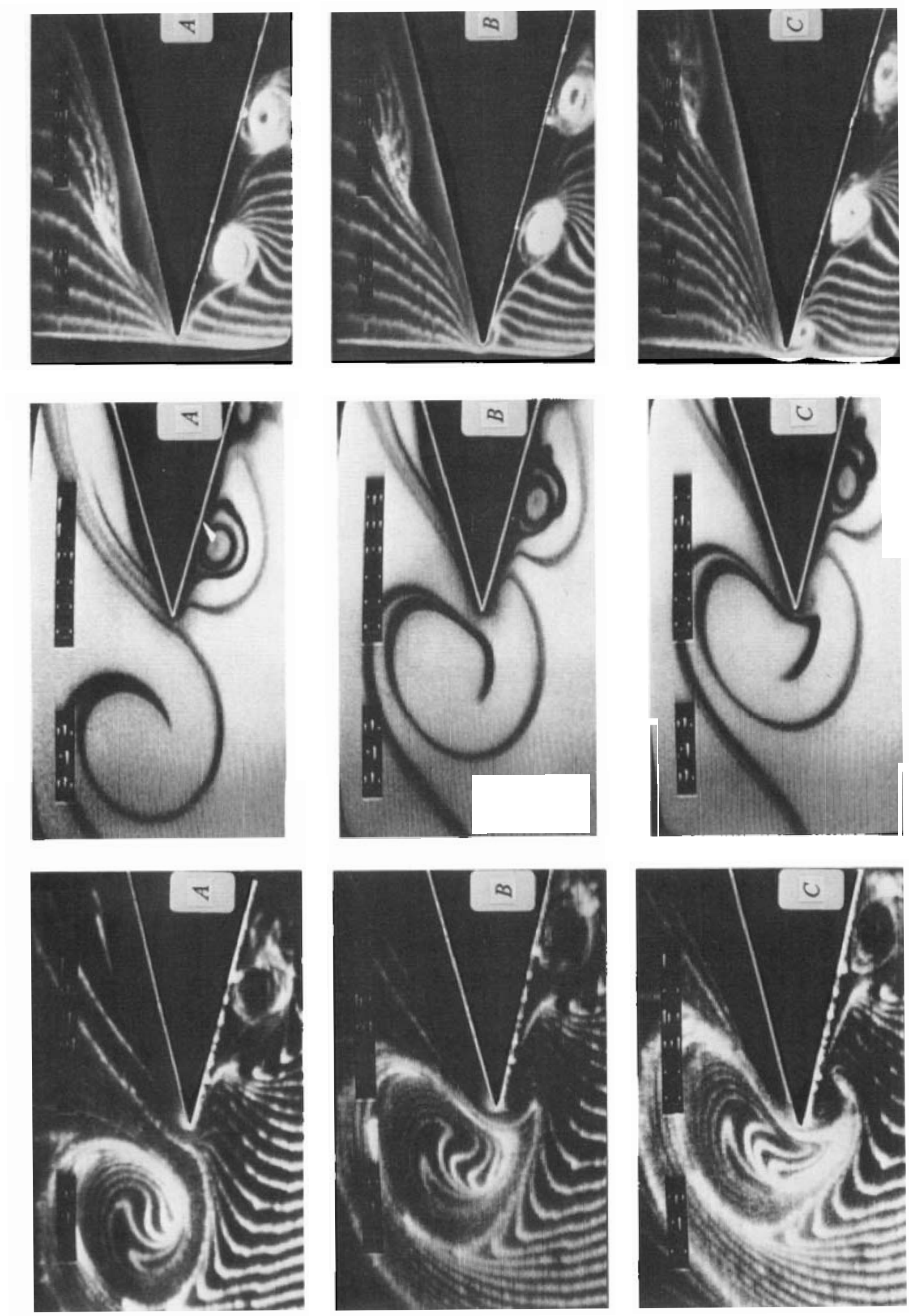
A
B
C
A
B
C
A
B
C

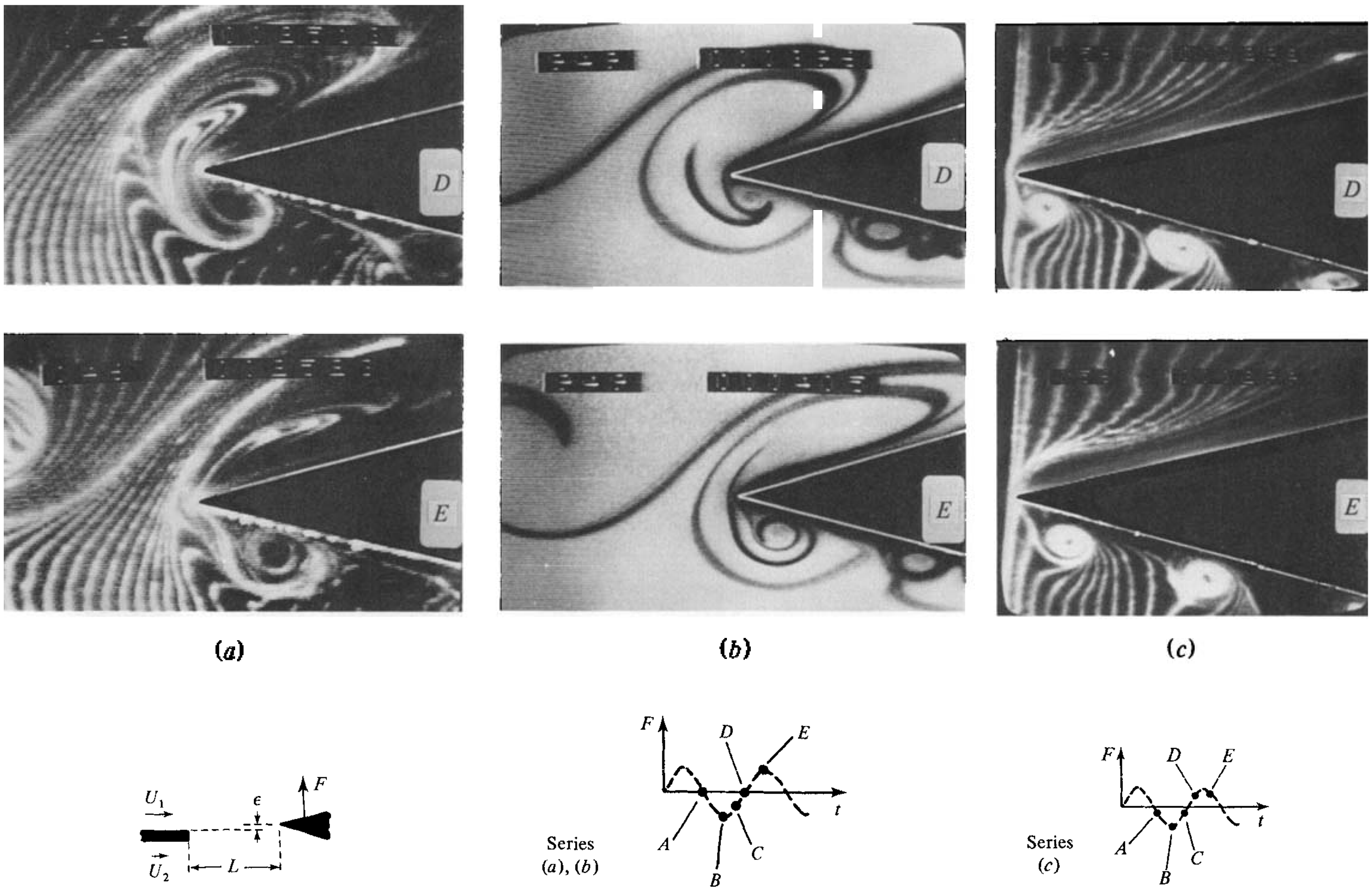

FIGURE 7. Visualization of vortex–leading-edge interaction for: (*a*) hydrogen-bubble wire located $21\theta_R$ upstream of wedge; (*b*) dye marker emanating from top edge of splitter plate; (*c*) wire located at leading edge. $R_{\theta_R} = 230$; $\epsilon/\theta_R = -1{\cdot}6$, $L/\theta_0 = 58$.

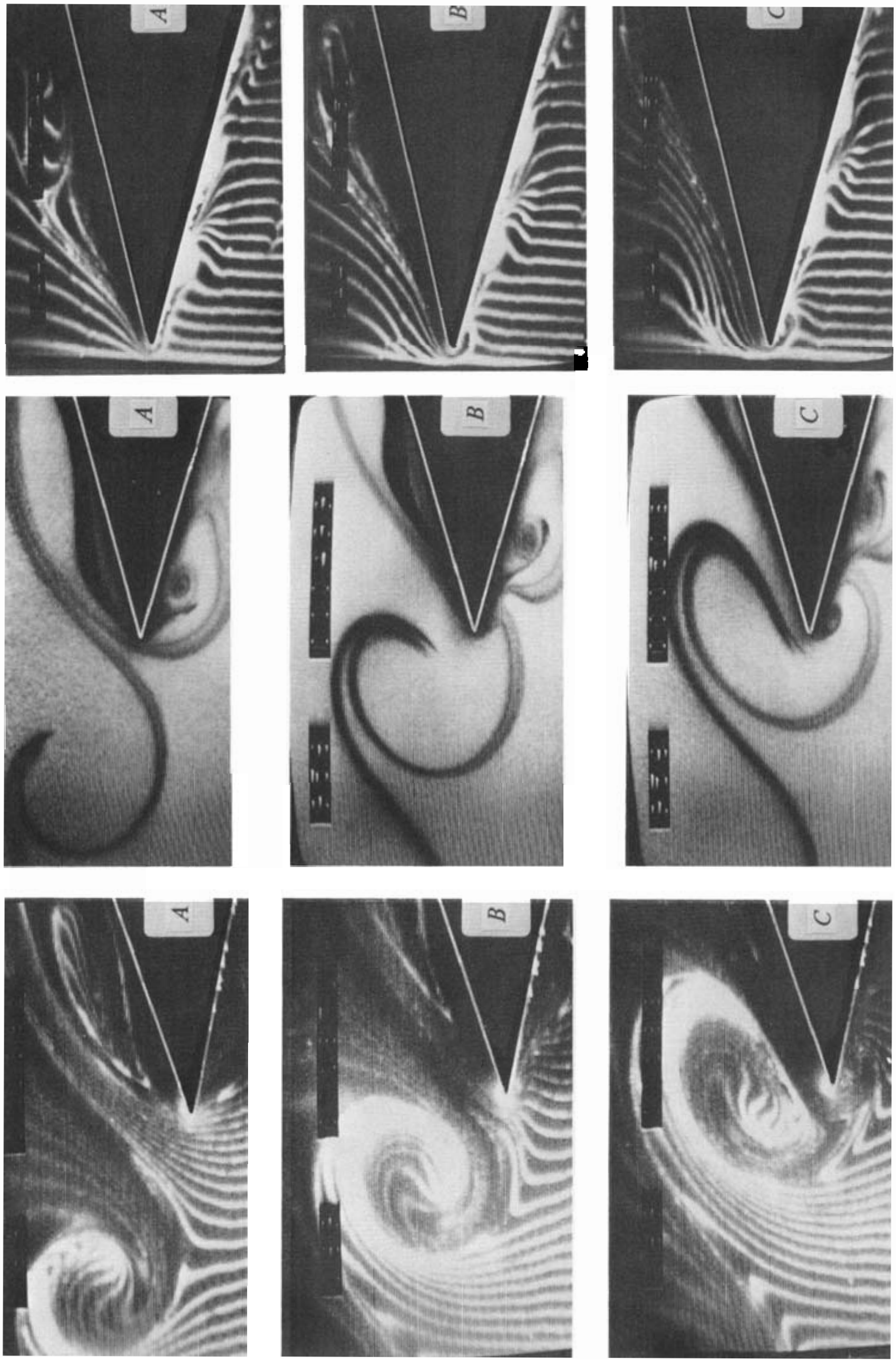
A
B
C
A
B
C
A
B
C

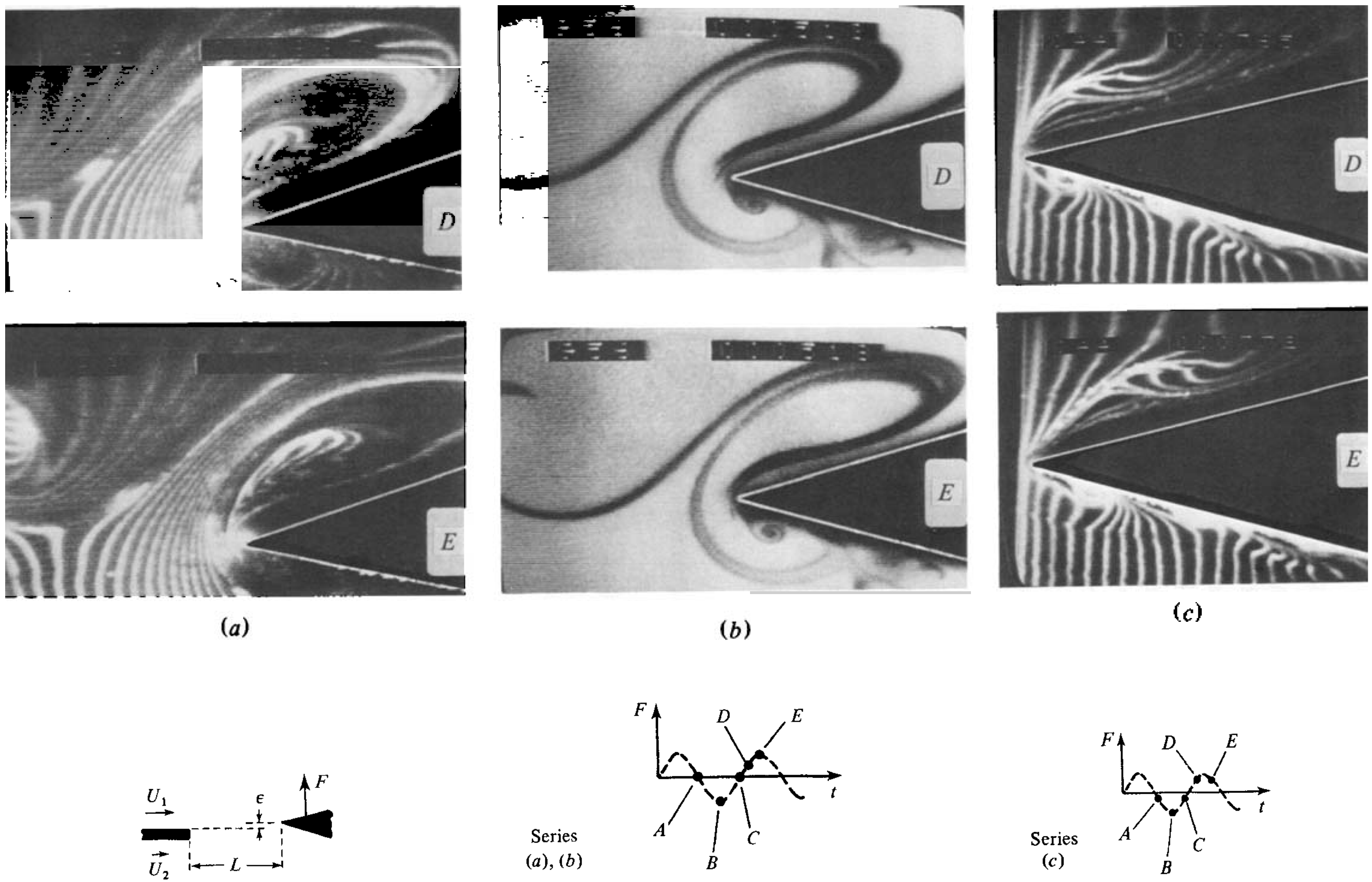

FIGURE 8. Visualization of vortex–leading-edge interaction for: (a) hydrogen-bubble wire located $21\theta_B$ upstream of wedge; (b) dye marker emanating from top edge of splitter plate; (c) wire located at leading edge. $R_{\theta_B} = 230$; $\epsilon/\theta_B = -2{\cdot}6$, $L/\theta_0 = 58$.

4. Mechanisms of interaction

Shown in figures 4–8 are the various interaction patterns as a function of transverse offset of the leading edge. For all values of offset, it is seen that as the vortex approaches the wedge, it tends to 'dive' beneath the leading edge. This can be seen by comparing frames *A* and *B* in figures 4 (*a*), 5 (*a*), 6 (*a*) and 7 (*a*). Even in cases when the centre of the approaching vortex is at a higher elevation than the leading edge (figures 6*a* and 7*a*), the most central portion of the vortex seems to be sucked rapidly to the underside of the edge during the later stages of the interaction process (observe the sequence t_C, t_D, t_E). This general feature is in agreement with the trend of the theoretical trajectories of *point* vortices addressed by Rogler (1974), and discussed in detail by Ziada (1981).

For the largest positive offset, $\epsilon/\theta_R = 1{\cdot}2$, shown in figure 4 (*a*), the major share of the distributed vorticity of the incident vortex is swept beneath the leading edge. Owing to the interaction of the vortex with the bottom part of the wedge, its foremost portion appears to be elongated in the streamwise direction; simultaneously a small-scale vortex of opposite vorticity (evident from corresponding films) is formed shortly downstream of the leading edge; this process is further apparent in figure 4 (*b*); the small-scale vortex becomes nested within the larger-scale incident vortex. In figure 4 (*c*), the shed vortex is barely discernible, appearing as a small white concentration of hydrogen bubbles.

Examining details of the central part of the incident vortex in figures 4 (*b*, *c*), there is a discernible tendency towards continued rotation of the inner portion of the incident vortex as it passes the leading edge and experiences elongation in the streamwise direction. The leading part of the dye marker in figure 4 (*b*) continues to move in a clockwise direction; and the timeline markers indicating the incident vortex in figure 4 (*c*) continue to evolve in the direction of a somewhat more-defined vortex (observe the sequence t_D, t_E, t_A, t_B in figure 4 (*c*)).

Concerning the force acting on the wedge, the maximum positive force occurs when the large-scale incident vortex and its nested vortex, originally shed from the leading edge, are well downstream of the leading edge, and before impingement of the next incident vortex. On the other hand, the maximum negative force occurs when the centre of the incident vortex is slightly upstream of the leading edge; these aspects will be quantified subsequently.

The case of a smaller positive offset, $\epsilon/\theta_R = 0{\cdot}2$, illustrated in figures 5 (*a*–*c*), reveals that the larger scale of the vortex shed from the leading edge imposes greater distortion of that portion of the incident vortex swept beneath the leading edge. Simultaneously, a larger fraction of the distributed vorticity of the incident vortex is swept above the leading edge. The larger scale of the shed vortex is further evident in figures 5 (*b*, *c*); moreover, in figure 5 (*c*), there is no clear evidence of continuation of 'roll-up' of the incident vortex downstream of the leading edge. The shed vortex appears to force together the distorted timelines associated with the incident vortex. However, the leading portion of the dye marker in figure 5 (*b*) indicates that the most central portion of the incident vortex continues to rotate clockwise after formation of the leading-edge vortex.

Concerning the upper region of the wedge, the timeline pattern of figure 5 (*c*) indicates a relatively thick region of vorticity, which is much thicker than the corresponding leading-edge viscous layer; apparently this is a result of the vorticity of the incident vortex being swept past the upper part of the wedge. In fact, the photos of figures 4 (*a*, *b*) and 5 (*a*, *b*) show that the upper portion of the vortex appears to be elongated in the streamwise direction, with no clear evidence of continued roll-up or further agglomeration. With respect to the instant at which the induced force attains its positive maximum, the shed vortex can be seen to be of larger scale and located closer to the leading edge than for the case of larger offsets described previously.

For the cases of negative offset, $\epsilon/\theta_R = -1{\cdot}0$, $-1{\cdot}6$, shown in figures 6 and 7, the tendencies described earlier become more pronounced; less vorticity of the incident vortex is swept beneath the leading edge (compare figures 5*a*, 6*a*, 7*a*); the shed vortex becomes stronger and of larger scale (figures 5*c*, 6*c*, 7*c*); the shed vortex is closer to the leading edge when the force is at its positive maximum (figures 5*a*, 6*a*, 7*a*); and the timelines near the upper edge of the wedge show stronger oscillatory patterns (figures 6*c*, 7*c*). Though there is still indication that the shed vortex is surrounded by distributed vorticity of the incident vortex (see figures 6*a*, 7*a*), the role of the shed vortex on the underside of the wedge clearly becomes more dominant. As will be discussed subsequently, this pronounced shedding of vorticity from the leading edge is associated with smaller relative amplitudes of induced force than in the case of positive offset.

However, if the offset of the leading edge is further increased in the negative direction by only one momentum thickness, to $\epsilon/\theta_R = -2{\cdot}6$, the scale of the shed vortex substantially decreases as shown in figure 8. This is accompanied by the major share of the vorticity associated with the incident vortex being swept past the upper surface of the wedge. The pattern of timelines in this region changes substantially with time, in contrast to patterns associated with large values of positive offset (see figures 4*c* and 5*c*); that is, the passage of the centre of concentration of vorticity originally associated with the incident vortex, is evident. In fact, a well-defined vortex is evident immediately downstream of the leading edge as can be seen from the sequence t_D, t_E, t_A of figure 8*c*.

5. Nature of shed vortex

A key feature of the leading-edge interaction is the nature of the vortex shed from the leading edge. This vortex shedding, which persists over a wide range of offset, appears to be strongest when the centre of the incident vortex is slightly above the leading edge. Furthermore, the shedding process seems to be further retarded as the vortex-edge offset is increased in the negative direction.

Flow separation from the leading edge can be discussed with the aid of figure 3 (*c*), which shows the r.m.s. amplitude of the transverse-velocity fluctuation $\tilde{v}(\beta)_{\mathrm{rms}}$ of Stuart's vortex versus the transverse location y. It can be seen that the maximum r.m.s. amplitude of $\tilde{v}(\beta)$, at the transverse location $y = 0$, is about 25 % of the velocity difference $\Delta\overline{U}$. During the first half of the cycle (i.e. leading half of the incident vortex), the incident vortex is still highly coherent, and this substantial transverse velocity should induce flow separation from the leading edge at its underside region. If the transverse-velocity fluctuation at the leading edge exerts the dominant influence during flow separation from the leading edge, consideration of the symmetrical distribution of $\tilde{v}_{\mathrm{rms}}(y)$ of Stuart's vortex would suggest that the separation angle, as well as the scale of the shed vortex, would be largest when the centre of the incident vortex is at the same elevation as the leading edge. The experimentally determined dependences

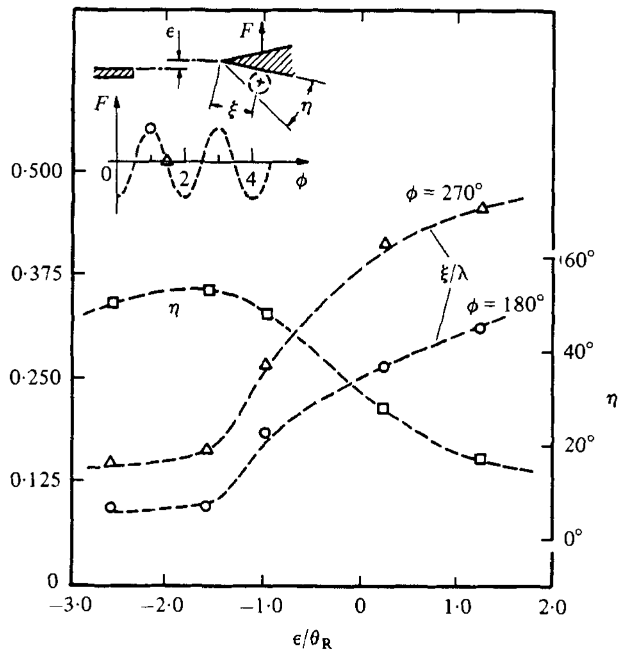

FIGURE 9. Angle of separation line η and position ξ of shed vortex as a function of wedge offset ϵ/θ_R.

of the separation angle and the streamwise position of the shed vortex on the value of offset are quantified in figure 9. The separation angle η is defined by the angle between the tangent to the separating part of the incident vortex and the underside of the wedge. This separation angle is most clearly depicted in the '*a*' series of the photos at time t_B for offsets $\epsilon/\theta_R = 1{\cdot}2$, $0{\cdot}2$ (figures 4*a*, 5*a*), and at time t_C for $\epsilon/\theta_R = -1{\cdot}0$, $-1{\cdot}6$ (figures 6*a*, 7*a*). Figure 9 shows that the separation angle is not largest for zero offset; instead, it is larger for negative values of offset, reflected in the larger scale of the shed vortex. Furthermore, figure 9 illustrates the retardation of the vortex-shedding process, relative to the induced force, for negative values of offset. In this plot, the distances of the shed vortex downstream of the leading edge for phase angles of 180° and 270° after the occurrence of maximum negative force, i.e. ξ_{180} and ξ_{270}, are plotted versus offset of the edge. As shown, the distance ξ at larger positive offset is typically three times that at the negative offset.

Thus the angle of separation from the leading edge, the scale of the shed vortex, and the axial location of the shed vortex are all intimately related. In the following, further examination of the vortex-shedding process, through visualization of the flow field just upstream of and at the leading edge, is addressed. The intent is to gain further insight into the influence of the transverse offset ϵ/θ_R of the incident vortex on the leading-edge shedding process.

The two extreme cases, $\epsilon/\theta_R = 1{\cdot}2$ and $-2{\cdot}6$, with the bubble wire at $8\theta_R$ upstream of the leading edge, are depicted in figure 10. Also shown are the disturbance streamline patterns, obtained by Rogler (1974), for a line vortex passing above and below the leading edge of a semi-infinite plate. For both cases, Rogler found the induced velocity to be relatively low in the geometric shadow blocked by the plate, while the velocity was infinite at the leading edge. Qualitatively, the streamline patterns indicate clearly that the induced velocity (due to the approaching vortex and its image inside the wedge) next to the upper wedge surface in case 2, i.e. when the vortex is above the leading edge, is much higher than that induced in case 1, i.e. when the vortex is below the leading edge. With regard to the experimental observations herein, this induced-velocity effect seems to be substantial for the case of negative offset. This is suggested in the flow-visualization photos of figure 10 (case 2) by the behaviour of the timelines in the region around the leading edge; somewhat retarded behaviour is depicted, as if there is a secondary (or local) flow around the leading edge from the upper side to the underside of the wedge. This effect is particularly evident for the case of $\epsilon/\theta_{\mathrm{R}} = -1{\cdot}6$ shown in figure 7 (*c*), where a small bulge in the timeline to the left of frame *C* is to be observed. This bulge appears during the initial stage of formation of the shed vortex (frame *B*), attains its maximum size midway through the shedding process (frame *C*); and starts to disappear when the shedding process is nearly completed (frame *D*). Similar, though less pronounced, behaviour can also be seen in figures 6 (*c*) and 8 (*c*). Clearly, for cases of negative offset, this mechanism produces a larger separation angle, and hence a larger vortex is shed.

In contrast with this case of relatively large negative offset, the interaction mechanism associated with a positive value of offset ($\epsilon/\theta_{\mathrm{R}} = 1{\cdot}2$) is shown in figure 10 (case 1); the vortex is seen to be swept much more smoothly past the leading edge, and no evidence of retarded flow at the upper side of the wedge can be observed. It appears that in the case of positive offset, the transverse velocity associated with the incident vortex dominates the process of vortex shedding, whereas in the case of negative offset this process seems to be dominated by the induction effects, which produce a low-speed region (or even a very weak, but discernible, reverse-flow region) next to the upper surface of the wedge.

Examination of series '*a*' and '*b*' of the photos (figures 4*a*, *b*–8*a*, *b*) reveals that leading-edge separation has occurred, and the very initial stage of vortex formation is underway for positive offsets ($\epsilon/\theta_{\mathrm{R}} = 1{\cdot}2$ and $0{\cdot}2$) at the instant of maximum negative force ($t = t_B$). In these cases, the shed vortex becomes well-defined at time $t = t_C$, about 45° after the occurrence of maximum negative force. On the other hand, for negative offsets ($\epsilon/\theta_{\mathrm{R}} = -1{\cdot}0, -1{\cdot}6$), clearly defined vortical structures are not evident until times $t = t_D$ or $t = t_E$, corresponding respectively to about 90° or 180° after the attainment of maximum negative force. This indicates relative retardation of the shedding process for negative values of offset.

A direct comparison of the shed-vortex trajectories for various values of leading-edge offset is given in figure 11. In constructing this plot, the distance ϵ of the shed vortex downstream of the leading edge, normalized with respect to the wavelength λ between incident vortices, was measured from the photos as a function of the induced-force phase angle ϕ_F, and all the trajectories were referenced to the phase angle at which the maximum negative force occurs, $\phi_{F_{\mathrm{max}-}}$. Different data points correspond to the three different methods of flow visualization, i.e. series '*a*'–'*c*' shown in figures 4–8.

In general, the convective speed of the shed vortex, given by the slope of the trajectory in figure 11 for sufficiently large phase angle ϕ_F, increases with increases in the offset in a positive direction. This general trend can be explained despite the complexity of the flow field near the leading edge. As the leading-edge offset is increased in a more positive direction, the shed vortex experiences a higher local mean velocity of the

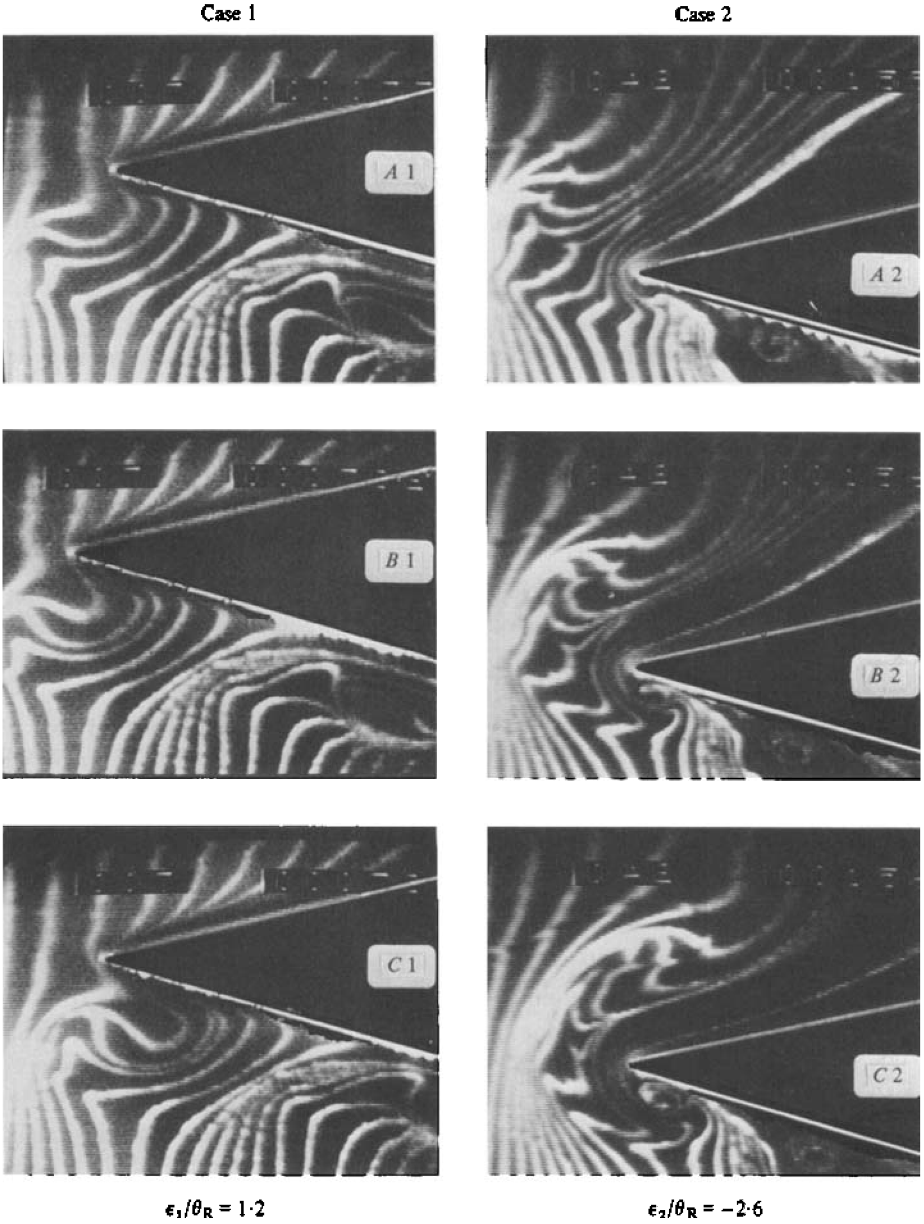

FIGURE 10. For caption see opposite.

incident shear layer, which is qualitatively compatible with the global behaviour of the shed vortex. However, calculations have shown that the local mean velocity seen by the shed vortex is consistently higher than its actual convective speed. The deviation between the vortex convective speed and its local mean velocity is largest when the shed vortex is strongest. Such features are indicative of the induction effects due to the shed vortex and its image inside the wedge. Induction effects are most pronounced, i.e. the deviation is largest, when the shed vortex is strongest. If there were no mean flow, the shed vortex would be convected *upstream* along the bottom surface of the wedge, around the leading edge, and then downstream along the upper surface of the wedge

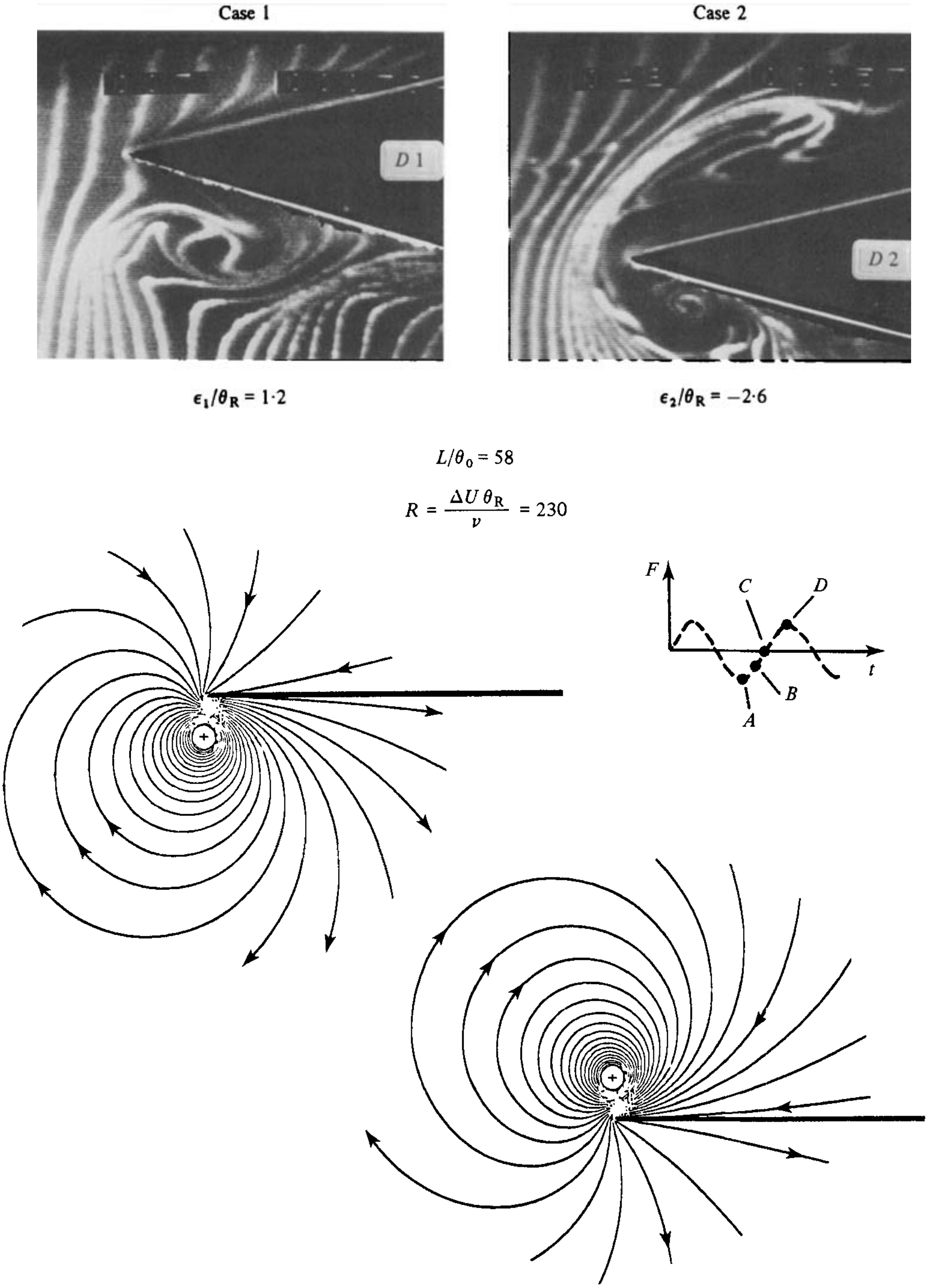

FIGURE 10. Comparison of vortex–leading-edge interaction for maximum positive offset ($\epsilon_1/\theta_R = 1{\cdot}2$) and maximum negative offset ($\epsilon_2/\theta_R = -2{\cdot}6$); hydrogen-bubble wire located at $8\theta_R$ upstream of wedge. $R_{\theta R} = 230$. Also shown are theoretical streamline patterns of point-vortex–leading-edge interaction (Rogler 1974).

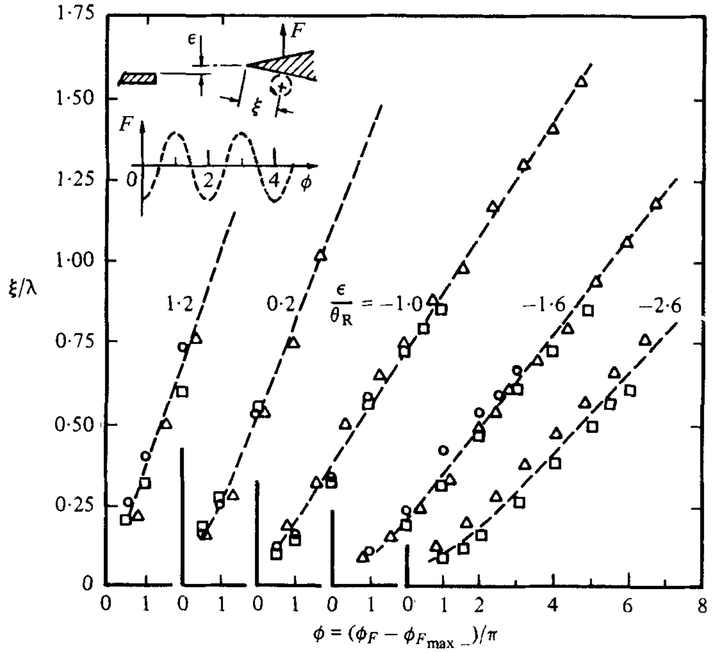

FIGURE 11. Distance ξ/λ of the shed vortex downstream of the leading edge as a function of phase angle of induced force $\phi_F - \phi_{F_{\max -}}$ for various values of offset ϵ/θ_R. Photo series: ○, '*a*'; □, '*b*'; △, '*c*'.

(Crighton 1975; Robertson 1965), with a convective speed directly proportional to its strength. Therefore the overall trend of the shed vortex trajectory can be attributed quite readily to a combination of local mean-velocity variation of the approach shear layer and induction effects.

6. Phase of induced force

The phase of the force exerted on the wedge, relative to the streamwise location of the incident vortex, is characterized at $\epsilon_{0\cdot5}/\theta_R = 0$ in figure 12(*b*), where $\epsilon_{0\cdot5}$ is the transverse offset between $y_{0\cdot5}$ and the leading edge of the wedge. Moreover, to examine the influence of the length scale of the sensitive part of the wedge (l/λ, where l and λ are defined in figure 12(*a*)) three different values of length scale were examined, as indicated in figure 12(*b*). In quantifying the phasing of events, the distance between the centre of vorticity concentration of the incident vortex and the leading edge of the wedge was measured from the video screen at the instant when the force attained its maximum negative value. At this instant, designated as $t = t_B$ in series '*a*' of the previously described photos, the centre of concentration of vorticity is located a distance Δ upstream of the leading edge (see figure 12*a*). The filled data points in figure 12(*b*) represent cases for which vortex pairing occurred upstream of the wedge, thereby producing a wavelength between vortices approximately twice that of the fundamental wavelength; open data points represent the case of a single incident vortical structure. Each data point represents the average of fifty independent events, recorded on the video system, for which the standard deviation was less than 15 % for

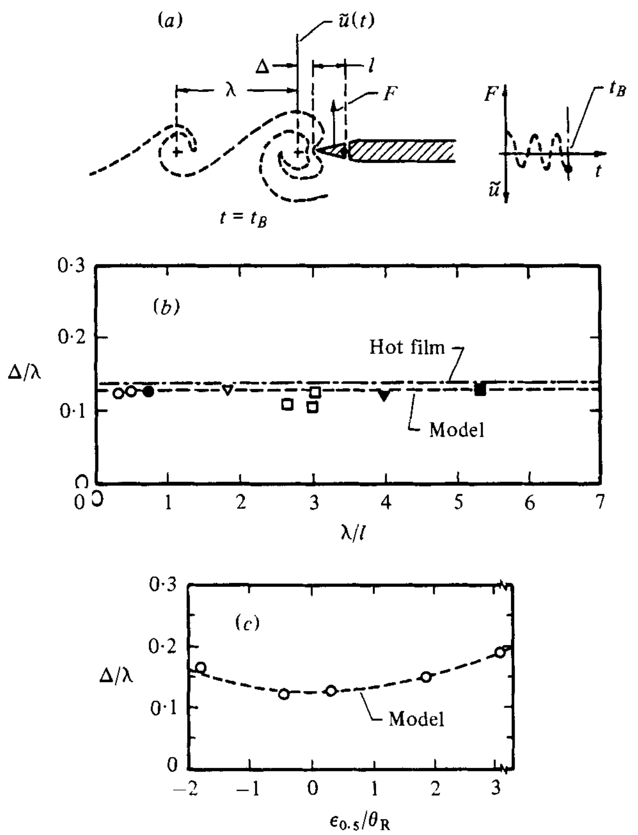

FIGURE 12. Distance Δ/λ of vortex centre upstream of leading edge at instant of maximum negative force on wedge ($t = t_B$): (*a*) definition of distance Δ; (*b*) Δ/λ *vs.* λ/l for $\epsilon_{0.5}/\theta_R = 0$ (○, $l = 6{\cdot}2$ cm; ▽, 1·4 cm; □, 1·0 cm); (*c*) Δ/λ *vs.* $\epsilon_{0.5}/\theta_R$ for $\lambda/l = 0{\cdot}39$.

all data points. Throughout the examined range of λ/l, the data indicate a *constant* nominal value of $\Delta/\lambda = 0{\cdot}12$.

In addition to the flow-visualization method, the phasing of the unsteady velocity signal was also used to quantify the distance Δ/λ. The hot-film probe was carefully traversed along the locus of the maximum r.m.s. amplitude of the streamwise velocity fluctuations until the velocity signal was 180° out of phase with the force signal (see figure 12*a*). Using this criterion, the distance of the hot-film probe upstream of the leading edge of the wedge, which corresponds to Δ, was measured and is depicted in figure 12 (*b*). This method of measuring the value of Δ was adopted in order to minimize the influence of local distortions of the incident vortex in the vicinity of the leading edge. The wavelength λ of the incident vortical structures was determined from the measured streamwise phase distribution of the velocity fluctuation, from the streamwise phase criterion for sustained oscillation, and from the screen of the video system. All methods yielded equal values of λ within $\pm 8\,\%$. The details of these phase measurements are discussed by Ziada & Rockwell (1981).

The fact that the distance Δ/λ does not vary significantly with dimensionless length of the wedge, λ/l, suggests that the major contribution to the force F is due to unsteady activity at, or in the immediate vicinity of, the tip of the wedge. In this regard, the aforementioned work of Rogler (1978) should be noted. He found that the amplitude of the fluctuating pressure exerted on the leading edge of a flat plate bisecting the inviscid vortical structure decreased with distance from the leading edge as $r^{-\frac{1}{2}}$. This predicted singularity in pressure at the leading edge is, in the laboratory, apparently relieved by vortex shedding from the leading edge. Although, as noted earlier, caution must be exercised in applying Rogler's results to the present investigation, because of his assumption of an array of square vortices, and neglect of leading-edge nonlinear and viscous effects, the concept of large amplitudes of fluctuating pressure at the leading edge is relevant to the present observation.

Since the mechanics at the tip of the leading edge is critical in determining the phase of the force fluctuation on the wedge, the previously described vortex model of Stuart should be capable of approximating some of the trends of phasing and relative magnitude of force fluctuations on the wedge. As shown in figure 3 (*c*), the r.m.s. amplitude of the transverse fluctuation velocity is a substantial fraction of the local mean velocity, suggesting that the transverse-velocity fluctuation at the leading edge is capable of exerting a dominant influence in determining the phase and the amplitude of the induced force fluctuation. Upon invoking the assumption that the induced force is proportional to the transverse velocity (i.e. to momentum) annihilated by the leading edge, the maximum negative force would be expected to occur when the transverse velocity at the leading edge is at a maximum negative value. Figure 3 (*b*) shows this to occur at a distance $\Delta/\lambda = 0{\cdot}125$ from the vortex centre. This value of Δ/λ, indicated in figure 12 (*b*) as a dashed line, is in good agreement with the measured values of Δ/λ. Furthermore, if the effect of transverse offset of the wedge, relative to the incident vortical structure is examined, a similar agreement between experiment and model is evident, as shown in figure 12 (*c*). In this plot, each data point represents the average of 30 vortex impingements recorded on the high-speed video system. The line representing the model is the streamwise location, relative to the vortex centre, at which the transverse velocity is at a maximum negative value; this predicted value of Δ/λ can be derived from (2), and is a function of $y - y_{0{\cdot}5}$ (i.e. a function of $\epsilon_{0{\cdot}5}$). This expression is given by:

$$\frac{\Delta}{\lambda} = \frac{1}{2\pi} \operatorname{arc\,cos} \frac{\alpha}{\cosh\left(2\pi\epsilon_{0{\cdot}5}/\lambda\right)}. \tag{5}$$

The good agreement between the model prediction, the hot-film measurements, and the flow-visualization data, which is evident from figures 12 (*b*, *c*), supports the assumption that the annihilation of local transverse momentum at the leading edge is central in determining the phasing between the vortex position and the induced force.

7. Amplitude of the induced force

Variation of the dimensionless force $F/F_{\max}$ as a function of the leading edge offset $\epsilon_{0{\cdot}5}/\theta_{\mathrm{R}}$ is given in figure 13. Even though the offset is varied by only a fraction of the reference momentum thickness ($\theta_{\mathrm{R}} = 0{\cdot}19$ cm), there is still a substantial reduction in the induced force relative to that induced at zero offset. In addition, for negative values of offset, the force drops off more rapidly than that for positive offsets; this is evident from comparing the induced force at $\epsilon_{0{\cdot}5}/\theta_{\mathrm{R}} \simeq -2$ with that induced at about $+2$. The dashed curve in figure 13 corresponds to that of figure 3 (*c*), representing the

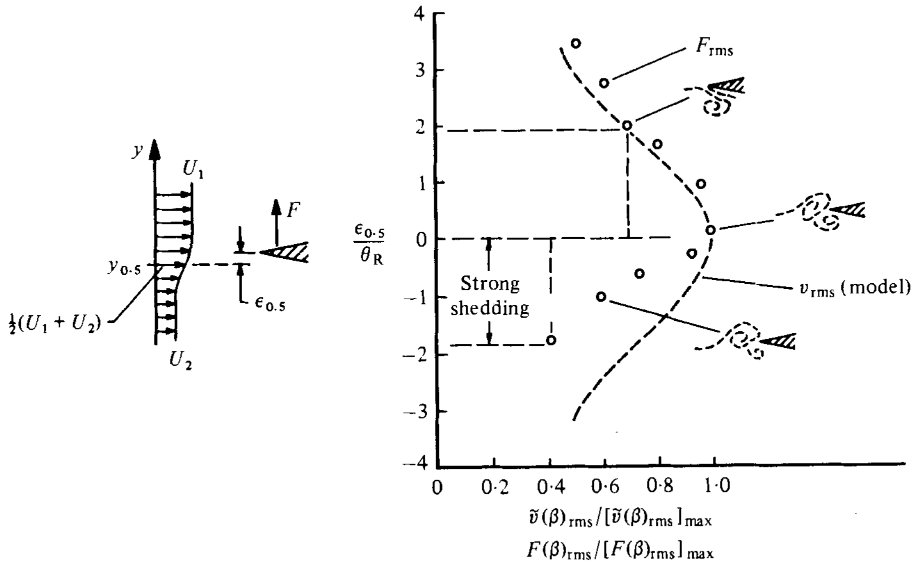

FIGURE 13. Variation of relative magnitude of force F/F_{max} as a function of offset of leading edge $\epsilon_{0\cdot5}/\theta_R$.

distribution of the transverse-velocity fluctuation amplitude calculated from Stuart's vortex model.

If the alteration in transverse momentum at the leading edge is central in determining the nature of the induced force, one would expect the variation of F_{rms} with the transverse offset $\epsilon_{0\cdot5}$ to follow the behaviour of $\tilde{v}(\beta)_{rms}$ in Stuart's vortex model. Figure 13 shows that this is indeed the case for positive values of offset. However, there is substantial deviation for negative offset, which is a consequence of the asymmetrical nature of the induced force. Recalling that the process of vortex shedding from the leading edge is stronger for negative offset, one is led to conclude that the shed vortex, which is not accounted for in the model, plays a more pronounced role at negative values of offset.

8. Concluding remarks

The inherent instability of the mixing layer generated by mixing two uniform streams, together with the upstream (feedback) influence of an impingement edge, sustained the formation of consistent and well-defined vortices with essentially identical characteristics, irrespective of the transverse location of the impingement edge in the mixing layer. Measurements taken during the state of amplitude equilibrium, i.e. in the region of nonlinear amplitude saturation, indicate that these vortices have an antisymmetric transverse (y) distribution of streamwise fluctuation velocity $\tilde{u}(\beta)$. This feature is in agreement with neutral modes of linearized theory and with Stuart's solutions of the nonlinear inviscid vorticity equation. Quantitatively, the features of the vortices formed upstream of the leading edge are well described by Stuart's (1967) vortex model when the vorticity concentration parameter α is set equal to 0·7.

The interaction mechanism between the vortex and the leading edge is found to be strongly influenced by small variations in transverse location of the leading edge with respect to the incident vortex. As the vortex approaches the wedge, it has a tendency to 'dive' to the underside of the leading edge. This behaviour is in agreement with the phenomenon of vorticity segregation pointed out by Rogler (1974).

For the considered range of transverse offset between the vortex centre and the leading edge, a vortex is shed from the leading edge towards the underside of the wedge. The frequency of the shed vortex is the same, but its vorticity orientation is opposite to that of the incident vortices. This shed vortex is stronger at negative values of offset, which accounts for the inducement of a smaller force than that induced at similar values of positive offset. It appears that at positive values of offset the process of vortex shedding from the leading edge is dominated by the transverse-velocity fluctuation of the incident flow, whereas at negative values of offset the vortex induction effects dominate, and retard the shedding process. Further features of the shed vortex, such as its phase and trajectory, are also considered in detail.

The induced force on the wedge, which has its largest amplitude at zero offset, drops rapidly as the leading edge is displaced in either direction away from the centre of the incident vortex. The interaction at, or in the immediate vicinity of, the leading edge is the major contributor to the induced force. These observations are in accord with Rogler's (1978) analysis, which shows that there is a pressure singularity at the leading edge and the fluctuation pressure amplitude decreases with distance r from the leading edge at the rate $r^{-\frac{1}{2}}$.

The position of the vortex centre upstream of the leading edge at which the wedge force had its maximum negative value was found to be a function of both the value of offset and the degree of vorticity concentration within the incident vortex. A simple model based on Stuart's exact solution, which accounts for the degree of vorticity concentration, can be used to predict the phase, i.e. the position of the vortex centre upstream of the leading edge at which maximum negative force occurs, as well as the relative magnitude of the induced force (for a certain range of wedge offset) as a function of the initial conditions of the incident vortex.

Examination of the agreement between the experimental observations and the addressed simple model makes clear that under certain conditions the model predictions show considerable inaccuracy. These conditions correspond to negative values of offset, whereby the shed opposite vortex dominates the underside of the wedge. The deviation arises because the model takes no account of viscous effects, which are associated with unsteady separation at the leading edge and a consequent shedding of the opposite vortex. This brings forth the need for further theoretical modelling to accommodate viscous as well as nonlinear effects.

The authors wish to express their gratitude to the National Science Foundation of Washington, D.C. and the Volkswagen Foundation of Hannover, West Germany for financial support of this investigation. They are grateful to Professor Charles Smith for the use of the high-speed video system and to Professor Mark V. Morkovin for helpful discussions.

REFERENCES

CONLISK, T. & ROCKWELL, D. 1981 Modelling of vortex–corner interaction using point vortices. Submitted for publication.

CRIGHTON, D. G. 1975 Basic principles of aerodynamic noise generation. *Prog. Aero. Sci.* **16**, 31.

ROBERTSON, J. M. 1965 *Hydrodynamics in Theory and Application.* Prentice-Hall.

ROCKWELL, D. & KNISELY, C. 1979 The organized nature of flow impingement upon a corner. *J. Fluid Mech.* **93**, 413.

ROCKWELL, D. & NAUDASCHER, E. 1979 Self-sustained oscillations of impinging free shear layers. *Ann. Rev. Fluid Mech.* **11**, 67.

ROGLER, H. 1974 A mechanism of vorticity segregation. *Bull. Am. Phys. Soc. Ser.* II, **19**, 1165.

ROGLER, H. 1978 The interaction between vortex-array representations of free-stream turbulence and semi-infinite flat plates. *J. Fluid Mech.* **87**, 3, 583.

STUART, J. T. 1967 On finite amplitude oscillations in laminar mixing layers. *J. Fluid Mech.* **29**, 417.

ZIADA, S. 1981 Self-sustained oscillations of a mixing layer–edge system. Ph.D. dissertation, Mech. Engng Dept, Lehigh University.

ZIADA, S. & ROCKWELL, D. 1981 Oscillations of an unstable mixing layer impinging upon an edge. Submitted for publication.